

Multi-redshift limits on the 21cm power spectrum from PAPER

Daniel C. Jacobs¹, Aaron R. Parsons^{2,8}, James E. Aguirre³, Zaki Ali², Judd Bowman¹, Richard F. Bradley^{4,5,6}, Chris L. Carilli^{7,10}, David R. DeBoer⁸, Matthew R. Dexter⁸, Nicole E. Gugliucci⁵, Pat Klima⁵, Adrian Liu^{2,11}, Dave H. E. MacMahon⁸, Jason R. Manley⁹, David F. Moore³, Jonathan C. Pober², Irina I. Stefan¹⁰, William P. Walbrugh⁹

ABSTRACT

We present new observations from the Donald C. Backer Precision Array for Probing the Epoch of Reionization (PAPER) telescope which place new deeper limits on the HI power spectrum over the redshift range of $7.5 < z < 10.5$, extending previously published single redshift results to cover the full range accessible to the instrument. The epoch of reionization power spectrum is expected to evolve strongly with redshift, and it is this variation with cosmic history that will allow us to begin to place constraints on the physics of reionization. The primary obstacle to this goal are bright foregrounds and the attendant systematics associated with high dynamic range measurements. Here we use filtering techniques that take advantage of the large instrumental bandwidth to make a high dynamic range subtraction of foreground power. Power spectra at different points across the redshift range reveal the variable efficacy of this subtraction. Noise limited measurements of Δ^2 at $k = 0.2 \text{ hMpc}^{-1}$ and $z = 7.5$ reach as low as $(48 \text{ mK})^2$ (2σ). Most spectra demonstrate a robust foreground removal of foreground signals to the thermal noise limit, leaving systematics on the scale of the noise. To better understand the source of these residual systematics we examine different estimates of the noise in the data and compare with theoretical predictions. We find that in the case of the highest redshift power spectrum, foregrounds begin to dominate over the

¹School of Earth and Space Exploration, Arizona State U., Tempe, AZ

²Astronomy Dept., U. California, Berkeley, CA

³Dept. of Physics and Astronomy, U. Pennsylvania, Philadelphia, PA

⁴Dept. of Electrical and Computer Engineering, U. Virginia, Charlottesville, VA

⁵National Radio Astronomy Obs., Charlottesville, VA

⁶Dept. of Astronomy, U. Virginia, Charlottesville, VA

⁷National Radio Astronomy Obs., Socorro, NM

⁸Radio Astronomy Lab., U. California, Berkeley, CA

⁹Square Kilometer Array, South Africa Project, Cape Town, South Africa

¹⁰Cavendish Lab., Cambridge, UK

¹¹Berkeley Center for Cosmological Physics, UC Berkeley, Berkeley, CA

noise, reflecting the increased difficulty in filtering foregrounds near the edge of the instrumental band.

Subject headings: reionization

1. Introduction

The Epoch of Reionization, when the first luminous objects ionized the pervasive cosmological hydrogen is predicted to be observable in highly redshifted 21 cm radiation. The Donald C. Backer Precision Array for Probing the Epoch of Reionization (PAPER, Parsons et al. (2010))¹ is a low frequency radio interferometer experiment dedicated to opening this window on the universe. Challenges include foregrounds which are brighter by several orders of magnitude and long integration times necessitated by the limited collecting areas of first-generation instruments. Direct observation of hydrogen before and during re-ionization is predicted to deliver a wealth of cosmological and astrophysical data, including the nature of the first stellar objects and the timing and rate of galaxy formation. Reviews on the physics of reionization as well as theoretical expectations on the nature of foregrounds may be found in Furlanetto et al. (2006); Morales & Wyithe (2010); Pritchard & Loeb (2012).

Other telescopes seeking to measure this signal include the Giant Metre-wave Radio Telescope (GMRT; Paciga et al. (2013)), the Low Frequency Array (LOFAR²; Yatawatta et al. (2013)) and the Murchison Widefield Array (MWA³; Bowman et al. (2013) and Tingay et al. (2013)).

PAPER is located in the Karoo desert at the site of the South African portion of the future Square Kilometer Array⁴ and has doubled in size on a yearly basis since 2009, and science-grade observations have been made with each stage of the build-out.

Here we report on deep integrations made with a 32 element array in 2011, first described in Parsons et al. (2014), hereafter P14. Our data reduction method was described in detail in P14, and used this pipeline to give the deepest yet limits on the HI power spectrum in the presence of bright foregrounds at redshift 7.68 using 92 nights (1800 hours) of data. The Epoch of Reionization signal is expected to evolve strongly with redshift, and it is this variation with cosmic history that will allow us to begin to place constraints on the physics of reionization (Pritchard & Loeb 2008; Pober et al. 2014). Therefore, while a detection of the 21 cm signal at even a single frequency would be a tremendous breakthrough, analysis techniques must be developed to capitalize on the wide

¹eor.berkeley.edu

²www.lofar.org

³mwatelescope.org

⁴skatelescope.org

bandwidths of the current generation of high-redshift 21cm telescopes. Using the same data set as P14, this paper presents improved upper limits on the HI power spectrum over the redshift range $10.7 > z > 7.2$. In Section 2 we summarize the observations, in Section 3 review the reduction methodology, we present the new upper limits in 4, and in Section 5 we offer conclusions and discussion of future work.

2. Observations

The work here follows the same basic procedure and uses the same underlying data set as P14. Here we provide a quick summary and refer the reader to P14 for a more in-depth discussion. A general overview of the PAPER system can be found in Parsons et al. (2010), calibration of the primary beam in Pober et al. (2012), and imaging results in Jacobs et al. (2011, 2013) and Stefan et al. (2013). Sensitivity analysis described in Parsons et al. (2012a) revealed that for the low gain elements employed by PAPER, a highly redundant “grid” type arrangement offers a significant sensitivity boost. In most interferometers the locations of the antennae are optimized such that each baseline samples a different Fourier mode of the sky; this is the ideal case for reconstructing images where each mode contains different information. For a power spectrum measurement the key metric is sensitivity per mode, rather than number of modes. A grid configuration allows many samples of each cosmological mode, to be averaged to a high sensitivity before being combined with other Fourier modes. The PAPER South Africa 32 antenna deployment (PSA32) was arranged in a 4×8 grid with a column spacing of 30m and a row spacing of 4m. In our analysis, as in P14, we include only the three shortest types of spacings where the reionization power is expected to be brightest. This selection includes those between adjacent columns and within at least one row of each other, a selection containing 70 ~ 30 m-long baselines. We will use these baselines to make a one dimensional estimate of the HI power spectrum.

Observations spanning the band between 100 to 200-MHz ($13.1 > z > 6.1$) were recorded at a resolution of 48kHz and 10.7s beginning Dec 7, 2011 and ending March 19, 2012 (with some down-time for maintenance) giving a total of 92 nights or 1800 hours. Within this set we included observations in the LST range 1h - 9h where the sky dominated system temperature is at a minimum. Note that this LST range is slightly shorter than in P14 which extended to LST of 12 hours. These last three hours were found to contribute minimally to increasing sensitivity while being dominated by bright galactic foreground emission and so have been excluded here.

3. Reduction

Here we summarize our data reduction steps; for more details see Section 3 of P14. In summary, we use 70 nearly identical baselines to make a 1D estimate along the spectral or line-of-sight direction of the reionization era HI power spectrum. All processing, save calibration, and the final

cross-multiplication step treats each baseline as independent. Foregrounds and interference are removed on a per-baseline basis with no a-priori sky model using signal processing techniques and a physical model of the array. In the final cross-multiplication step, the last layer of systematics is estimated and removed by projecting non-physical correlations between baselines.

3.1. Delay and Fringe rate transforms or The Fourier Furor

In several stages throughout the analysis process we take a 2D Fourier transform of the visibility spectra $V(\nu, t)$ into “delay/fringe rate” space where delay is the Fourier dual to frequency and similarly fringe-rate for time. In this space, smooth spectrum sources are physically localized to delays shorter than the light travel time length of the baseline and fringe rates shorter than the angular sidereal rate perpendicular to the baseline vector. Sources at the horizon, in the direction of the baseline vector, have the longest delays, while fringe rates are highest where the celestial equator crosses the horizon.

In this Fourier space, sources are highly localized with deviations from a flat spectrum manifesting as a slight dispersion. The spectrum sampling function, which is uneven due to flagging of interference takes the form of a convolution by a point-spread-function (PSF) in the same way an imperfect sampling of the uv plane gives rise to the angular PSF of an interferometer. If enough data is missing this PSF can cause smooth-spectrum sources to leak beyond the horizon. To account for this, we use a CLEAN like, iterative, peak-finder and subtraction algorithm which is limited to finding peaks within the physically allowable ranges of delay and/or fringe-rate. In this case, the 1D “CLEAN” beam is the Fourier transform of the spectral or time sampling function (Parsons & Backer 2009).

The data analysis pipeline essentially consists of iterative application of the delay or fringe-rate transform process, with an ever tightening allowable number of modes, interleaved with stages of averaging (time, frequency, night), before finally computing a power spectrum. This final step takes advantage of the redundant baselines to make an unbiased power spectrum estimate by cross-multiplying identical baselines and then averaging the power spectrum modes. By not combining baselines until the last step and by assuming that the line of sight transform is well approximated by the delay transform we dramatically simplify the analysis procedure to a series of signal processing steps. It also obviates the need for precision sky and instrumental beam models which are required by imaging arrays.

This isolation of foregrounds to a region below a line-of-sight k_{\parallel} mode that increases with baseline length is also the much discussed “wedge” Liu et al. (2014a,b); Thyagarajan et al. (2013); Pober et al. (2013a); Trott et al. (2012); Morales et al. (2012); Parsons et al. (2012b); Vedantham et al. (2012); Datta et al. (2010); Parsons & Backer (2009). As we only have a single length of baseline the wedge manifests as a single value of $k \sim k_{\parallel}$, below which foregrounds are expected to dominate. The details of each application of the delay/fringe-rate transform will be laid out the

following sections as we provide a brief walk-through of the processing pipeline.

3.2. Selection of Redshift Bins

The redshift bins for which we have computed power spectra –shown in Figure 1– have been selected from the available bandwidth using two criteria: minimizing covariance between redshifts and avoiding missing data. We minimize covariance between adjacent redshift bins by limiting overlap of each bin to the spectrum at the outer half of the bin channel range which, as will be described in section 3.6, is significantly down-weighted by the use of a Blackman-Harris window. Avoiding missing data is important because the power spectrum method, developed in P14, which leverages the redundant baselines to estimate non-sky covariance and project out these contaminated modes is particularly sensitive to missing data –the inverse of the covariance is not defined– so we also select only channels that have no missing data over the entire sidereal period (see the dotted line in Figure 1). With these constraints we arrive at the redshifts 10.3, 8.5, 7.9 and 7.45. For the purposes of comparison with P14 we also include the redshift 7.68 bin. Dillon et al. (2013) describes a pseudo-inverse method for handling the covariance introduced by missing data. Though not implemented here, this method is in the process of being adapted for use in highly redundant analysis (Liu et al. 2014a,b).

The spectral width of the redshift bins is dictated by two competing needs. First, sensitivity and foreground reduction both benefit from wider bandwidths. On the other hand, power spectrum measurements which trace the evolution with redshift require smaller bandwidths. Often, the evolution scale is taken to be on order $\Delta z \approx 0.5$, which translates to a bandwidth limit $B < 0.5(f^2/1421)$ MHz. To balance these two competing constraints we choose a single spectral bandwidth of 20MHz, weighted by a Blackman-Harris window for an effective width of 10MHz, or $\Delta z = 0.5$ at $z = 7.45$ ranging up to a $\Delta z = 0.86$ at redshift 10.3.

3.3. Initial Averaging

First, the raw data are down-selected to just the 70 30m long baselines described in Section 2. The visibilities are then compressed in the frequency and time directions by removing delay modes and highest frequency fringe rates corresponding to a 300m baseline (the longest baseline in the array). This filtering⁵ is done in tandem with a radio frequency interference (RFI) flagging step, using the residuals which have had bright sky-like signals removed to flag 4σ deviations before feeding the flags back into another iteration of the compression step. This mitigates the effects of bright, narrow band, interference being scattered into higher delay modes (where reionization lives) and results in a time and frequency bin of length 39.6s and width 492.61kHz. This process reduces

⁵See Appendix A of P14

the data volume by a factor of ~ 20 , or roughly an order of magnitude improvement on traditional time and frequency averaging which in this array would be limited to 100kHz and 10s to avoid averaging away fringes.

3.4. Calibration

We model the gain as a per-antenna amplitude and a phase slope -physically a single time delay- and single real, low order polynomial passband for all antennae. Because the array samples correlations redundantly, the relative calibration between antennae is numerically overdetermined and tractable as a linear algebra problem (Liu et al. 2010). As described in P14, we compute the ratio between redundant baselines, fit for a gain and phase slope and then algebraically solve for a per-antenna solution. Using this method we have avoided calibrating each channel independently to preserve as much frequency variation as possible. These solutions vary little over the three month observing period, exhibiting less than 1% r.m.s. variation. A single solution derived for the Dec 7 data set is used for the entire observing run. Time and frequency variation of redundant solutions is explored in general in Zheng et al. (2014).

Relative calibration is all that is necessary to form a power spectrum. To obtain a correctly normalized power spectrum, however, it is necessary to set a flux scale for which we need a flux measurement of a calibration standard. For this we form a beam on a known, bright calibration source. However, by itself the redundant calibration does not contain enough phase information to phase coherently to a sky location, there remain two free phase parameters which cannot be solved by redundancy alone. We find these by fitting a model of Pictor A, Fornax A, and the Crab Nebula during a time when the sky is dominated by these three sources while marginalizing over the unknown⁶ apparent flux ratio between the three sources. With the delays in place we are now able form a beam on Pictor A and (for each channel) set the overall amplitude to the calibration value of $382 \text{ (f/150MHz)}^{-0.77} \text{ Jy}$ found in Jacobs et al. (2013).

3.5. Foreground Filtering and Night Averaging

Foregrounds are filtered from the calibrated data by removing all bright delay components with light travel times less then the baseline length. Where during the previous compression step a liberal horizon of 300m (1800ns, much longer than the 30 meter baselines under study) was used to calculate the window size, we now choose a window corresponding to the 30m baselines under study with an extra buffer of 15ns to provide a slight buffer against the $1/B \sim 12\text{ns}$ resolution of the

⁶Unknown in the sense of a joint uncertainty in source flux and primary beam pattern. Though the fluxes of these sources is in some cases fairly well constrained, fluxes at 150MHz are still fairly uncertain as is the PAPER beam in those directions.

delay spectrum. The broadband delay spectrum model is iteratively built then subtracted from the data leaving residuals which we carry into the next stage. Next, a four hour long running mean is subtracted. This removes excess correlation due to cross-talk in the analog signal chain. The residuals are then flagged once more for RFI before the 92 nights of data are averaged into 36.4 second long local sidereal time (LST) bins, which as PAPER is a drift-scanning instrument, are equivalent to bins in Right Ascension (Declination is fixed at -30°). During averaging we found that some LST bins were dominated by a small number of exceedingly bright samples lying well outside the rest of the gaussian distributed data. To compensate we filter the 10% brightest samples in each bin. The source of these outliers is not known, a likely possibility is an instability in the analog signal chain stimulated by weather or bright interference, a circumstance that has since been observed in later seasons.

Though the frequency and repeated nightly observations have been averaged to their maximum extent, at 40s integrations the time axis has yet to be fully exploited. Sky-like fringes on a 30m baseline rotate much slower than 40 seconds. Performing a final fringe-rate filter, limiting to fringe-rates expected on a 30m baseline (down from 300m in the last iteration), we arrive at a data-set averaged to 789s, the maximum possible while still maintaining fringe coherence. The root mean square of the residual signal (seen in Figure 2) at the end of this process is close to the 3mK level expected given the total integration time and system temperature.

3.6. Power Spectrum

The output of the above steps is a single calibrated and foreground filtered sidereal night of visibility data. The power spectrum is estimated in the delay spectrum of a 10MHz bandwidth range centered on the redshift of interest. To preserve the isolation of any foregrounds which remain, we increase the spectral range by 5MHz on each side and multiply by a Blackman-Harris window thus providing a much higher dynamic range delay spectrum point spread function.

This leaves us with 40 delay samples on each of 70 baselines which are divided into three redundant groups. Within these groups we cross correlate delay spectra between different redundant baselines. The cross multiplication of the same delay modes between different redundant baselines provides an unbiased estimate of the power spectrum. These "sky-like" correlations should be identical between all redundant baselines to within the level of the noise, while all other cross multiplications between delay modes should not be correlated between different baselines. In practice these non-sky-like modes do occasionally have significant power which leaks into the correlations which sample the power spectrum. These are removed by iteratively dividing the covariance into a model of systematics and a model of sky-like emission and then projecting out large residual modes. This is done by dividing the baselines into different groups such that all cross-multiplications are done without introducing noise bias. For more see Appendix of C of P14.

The residual elements of the correlation matrix corresponding to cross-multiplication of match-

ing delay bins between different baselines are all un-biased samples of the power spectrum. To estimate the final power spectrum and its uncertainty we compute the mean and variance of many random randomly-selected subsamples, sampling the dimensions: sidereal time, redundant baseline pair, and delay sign⁷.

4. Results

4.1. Foreground Filtering and Noise Levels

The root-mean-square of the filtered visibilities measures how well we’ve removed foregrounds. In Figure 2 we examine T_{rms} as calculated by differencing between adjacent channels and between redundant baselines. We see that in the last stage of coherent integration, the step between 40 second to 789 second integrations, the noise level decreases by the expected factor of $\sqrt{789/40}$. At both stages the noise level found by both methods is roughly consistent with the theoretical level, only deviating significantly at the edges where the effective signal to noise due to the decreasing passband gain, Blackman Harris window, and uneven sampling (see Fig 1) drops precipitously.

The theoretical visibility r.m.s. noise level is a straightforward calculation, but given the method employed here, should be given due description. The noise level in a long integration (Eq. 4.1) is caused by the temperature of the sky (mostly due to galactic emission) which varies with LST and by the receiver noise, both on the scale of a few 100K. The noise of any long integration is also dependent on the number of observations in each LST. The number of points in each bin is mostly determined by the observing schedule, which for PAPER is sunrise to sunset, but also by any flagging of data or observing outage (only 92 of the 103 days in the observing period have recorded data). Unfortunately, technical problems limited the retention of the exact cumulative count of points averaged into each LST bin during the averaging process. Here we have chosen to use the first order estimate based on the observing schedule to estimate the number of observations in each LST. Some bins are observed only a few times, while a slim range in the LST range 6 - 9 hours is observed on every night. Over a number of LST bins N_{lst} the average effective time per bin N_{eff} is given by

$$\frac{1}{\sqrt{N_{eff}}} = \left\langle \frac{1}{\sqrt{N(lst)}} \right\rangle_{lst}$$

On average each bin in this dataset is effectively measured 39.6 times. Given this accounting of the number of samples $N(lst)$, we estimate the r.m.s. temperature of the averaged data set to be

⁷As visibilities are complex, both the positive and negative delays carry information. Physically the two signs correspond to the two halves of the sky.

$$T_{rms} = \frac{1}{N_{lst}} \sum_{lst} \frac{T_{sky}(lst) + T_{rcvr}}{\sqrt{2BtN(lst)}} \approx \frac{(< T_{sky} > + T_{rcvr})}{\sqrt{2BtN_{eff}}}$$

where B and t are the 496kHz channel width and lst bin length, respectively and the approximation indicates that we have assumed average values for the number of samples and the time dependent sky component of the system temperature. In P14 the total system temperature ($T_{sky} + T_{rcvr}$) was estimated to be 550K using 20 nights of the 92 night set which covered LSTs 3-9. Using the global sky model (de Oliveira-Costa et al. 2008) and a model of the PAPER primary beam we estimate the mean T_{sky} during that 20 night period to be 250K, implying a receiver temperature of 300K. The mean temperature over the full 92 night period is only 4K higher; the estimate of 550K for the system temperature is a good estimate for the full observing period. T_{rms} using 550K and an effective sample count of 39.6 is plotted as a dotted line in Figure 2 for before and after fringe rate filtering (t=40s and 789s)

The final fringe-rate step is the last coherent average of the processing routine and represents the last large gain in sensitivity; all following averaging steps are done incoherently on the square of the visibilities where sensitivity is gained at a much slower rate. For this reason the noise curves (bottom three curves of Figure 2) merit closer inspection. At this sensitivity level we see a notable excess of power in the r.m.s. difference between baselines. Though the cause of this excess is unknown, it is suggestive of the excess covariance between redundant baselines which we remove in Section 3.6 a hypothesis also supported by the high levels of residual foregrounds in the redshift 10.5 bin where the baseline difference r.m.s. is highest.

4.2. Power Spectra

In Figure 3 we show the power spectra at different redshift bins –showing both the spherically averaged power spectrum $P(k)$ and the volume independent $\Delta^2(k) \equiv \frac{k^3}{2\pi^2} P(k)$. The $P(k)$ spectrum averages the three baseline types but preserves the positive and negative delays. In figure 5 we see different k mode slices as a function of redshift, all plotted with 2σ error bars and in Table 1 we list the data plotted in these slices.

The theoretical noise power spectrum (dashed line in figures 3 and 4 and grey region in figure 5) is estimated using the method described in Poher et al. (2013b), assuming a system temperature of 550K and the observing scheme described in Section 2. In all figures the noise levels are plotted for comparison with the power spectrum values rather than the error bars, i.e. 65% of uncorrelated points should lie below the line or within the grey region. In general the theoretical error bars are larger than the bootstrap errors. This is probably most clear in 5 where, though most points are inside the error region, the bootstrap errors are only consistent with zero 25% of the time. In general it would appear that the sensitivity calculations under-estimate the sensitivity of the measurements by a small factor. See Poher et al. (2014, 2013b) for a discussion of the approximations made in

those calculations.

Generally, both figures convey a picture of a power spectrum dominated by noise, with foregrounds encroaching from inside and just outside the horizon to higher k “reionization” modes. One easy way to see this leakage is by comparing the bootstrap error bar, the theoretical error and the power spectrum value. At the level of noise here, we expect all points outside the horizon to be consistent with zero. As a simple sorting criteria we divide the points into “Detections” and “Upper Limits” (Det/ULim) in Table 1 for both theoretical and bootstrap error bar. As we can see, the larger theoretical error bars are mostly consistent with zero, while the same is true of a little less than half of the bootstrap error bars. This is consistent with a picture of systematics or foreground leakage near the thermal noise limit.

Foreground dominance appears to grow with increasing redshift, mirroring the rise in baseline-to-baseline r.m.s. we found in Figure 2. Recall that the wide-band foreground model we have subtracted –which causes the notch of missing power⁸ near $k_{\parallel} = 0$ in Figure 3– is the same for all redshift slices and was built by weighting the entire band by a Blackman-Harris window function. Using this window, contributions to the foreground model from 126MHz ($z = 10.3$) are down-weighted $\sim 75\%$ compared to 150Mhz ($z = 8.47$). If the 126MHz sky or systematics are much different then 150Mhz foreground residuals at that redshift will be higher. The $k = 0.1 \text{hMpc}^{-1}$ slice (upper left of figure 5) is only a factor of \sim three away from the light travel horizon of $k = 0.035$ and therefore most likely to be contaminated by low k foregrounds. This k mode is well above the noise and has a redshift dependence much the same shape as the T_{rms} curve in Figure 2, with a minimum near redshift 8.5 and a dramatic rise above redshift 10.

5. Conclusions

The power of the highly redshifted 21 cm as a cosmic probe lies in its ability to probe a 3D volume by observing at different frequencies. The present analysis extends the work of Parsons et al. (2014), which used a single-baseline delay spectrum analysis to place an upper limit on the 21 cm power at $z = 7.68$ (163 MHz). In this work, we take advantage of the wide bandwidth of the PAPER instrument to place limits on the power spectrum at a range of redshifts $10.7 > z > 7.2$, demonstrating that the algorithms used in P14 can exploit the full potential of the 21 cm line.

Most of the power spectrum data points demonstrate a removal of foreground signals to approximately the thermal noise limit, leaving systematics on the scale of the noise. Noise limited bins –those which are statistically consistent with zero and marked as ULim in Table 1– occur at several k modes at redshifts 7.55, 7.94 and 10.29. The deepest point –at redshift 7.55 and $k = 0.2$ – is a 2σ upper limit of $(48 \text{mK})^2$. For comparison, the Lidz et al. (2008) fiducial model of the reionization power spectrum estimates an amplitude of $(4.4 \text{mK})^2$, for models with 50% reionization at $z = 7.55$.

⁸Note that this notch is not present in figure 4 because the foregrounds have been left in for comparison with P14.

Table 1. Power spectrum values

k	redshift	Δ^2	bootstrap error	noise model	bootstrap	noise model
[hMpc ⁻¹]		[mK ²]	[mK ²]	error	significance	significance
				[mK ²]		
0.1	10.29	43575.5512	± 5729.3347	± 8029.1131	Det	Det
0.1	8.54	5701.6267	± 1168.7025	± 3671.887	Det	Det
0.1	7.94	7695.373	± 2044.5824	± 3133.8433	Det	Det
0.1	7.55	9461.8178	± 2761.5645	± 2393.1972	Det	Det
0.2	10.29	11410.9746	± 5039.8271	± 27281.158	Det	ULim
0.2	8.54	5855.8909	± 2195.8363	± 12275.7791	Det	ULim
0.2	7.94	5143.6577	± 1799.7316	± 10221.3583	Det	ULim
0.2	7.55	856.316	± 1490.2202	± 7636.2256	ULim	ULim
0.3	10.29	34756.4662	± 16384.7719	± 64977.9446	Det	ULim
0.3	8.54	12923.2987	± 5373.4928	± 29058.6627	Det	ULim
0.3	7.94	5204.3757	± 4834.4927	± 24046.4004	ULim	ULim
0.3	7.55	7628.4564	± 4810.3274	± 17762.1184	Det	ULim
0.4	10.29	42909.9827	± 30695.0274	± 128355.9988	ULim	ULim
0.4	8.54	24115.248	± 16585.6317	± 56571.7524	Det	ULim
0.4	7.94	14730.7401	± 9930.2065	± 46725.4956	Det	ULim
0.4	7.55	-8601.8091	± 14191.4889	± 34339.7156	ULim	ULim

^aDet indicates a measurement and error-bar inconsistent with zero, ULim indicates consistency with zero at 2σ .

The fact that the best upper limit still comes from the $z = 7.6$ band does illustrate that this redshift corresponds to a somewhat special frequency for the PAPER instrument, where the combined contribution of system noise, RFI signals, and residual foregrounds (if any remain) are at a minimum.

Further work will look to expand on this result on several fronts. Alternative algorithms to the wide-band CLEAN could potentially better remove the delay-space covariance introduced by RFI flags in frequency and are under investigation. Another active point of investigation is aimed at alternative windows to the Blackman-Harris used in the wide-band CLEAN (or wholly distinct algorithms) that could better remove foregrounds from the edges of the band while still limiting foreground bleed into the EoR window.

Future work will also include observations from subsequent seasons with more antenna. The observations reported here demonstrate a nearly noise limited integration over a full season but used only a quarter of the final design antenna count. These 32 antenna observations from 2011 were followed by a full season of 64 antennae in 2012 and 128 in 2013. A second season of observing with the 128 antenna array is now under way. In going from 32 to 128 antenna the mK^2 sensitivity increases by the expected factor of 4 and by an additional factor of ~ 2 after accounting for the substantial uv-plane redundancy (Parsons et al. 2012a).

The analysis of the system temperature presented in section 4.1 is one of the most thorough such investigations applied to the PAPER instrument. It confirms the effectiveness of the wideband CLEAN in removing foregrounds over a wide range of the band, while illustrating weaknesses in this approach in pushing towards the edges of PAPER’s frequency range. Furthermore, after the application of the fringe rate-based time averaging, we see hints that baseline-to-baseline variations between redundantly spaced baselines is becoming the dominant systematic in the analysis. Techniques like the covariance removal introduced in P14 and also used in this work can differentiate some of this variation from the sky signal; however some combination of improved calibration techniques (Zheng et al. 2014), model building (Sullivan et al. 2012), and a better understanding of error covariance (Liu & Tegmark 2011) may also prove valuable in reducing this systematic.

REFERENCES

- Bowman, J. et al. 2013, Publications of the Astronomical Society of Australia, 30, 31
- Datta, A., Bowman, J. D., & Carilli, C. L. 2010, The Astrophysical Journal, 724, 526
- de Oliveira-Costa, A., Tegmark, M., Gaensler, B. M., Jonas, J., Landecker, T. L., & Reich, P. 2008, Monthly Notices of the Royal Astronomical Society, 388, 247, (c) Journal compilation © 2008 RAS
- Dillon, J., Liu, A., & Tegmark, M. 2013, Physical Review D, 87, 43005

- Furlanetto, S. R., Oh, S. P., & Briggs, F. H. 2006, *Physics Reports*, 433, 181, elsevier B.V.
- Jacobs, D. et al. 2011, *The Astrophysical Journal*, 734, L34
- Jacobs, D. C. et al. 2013, *The Astrophysical Journal*, 776, 108
- Lidz, A., Zahn, O., McQuinn, M., Zaldarriaga, M., & Hernquist, L. 2008, *The Astrophysical Journal*, 680, 962
- Liu, A., Parsons, A. R., & Trott, C. M. 2014a, eprint arXiv, 1404.2596
- . 2014b, eprint arXiv, 1404.4372, 19 pages, 7 figures
- Liu, A. & Tegmark, M. 2011, *Physical Review D*, 83, 103006
- Liu, A., Tegmark, M., Morrison, S., Lutomirski, A., & Zaldarriaga, M. 2010, *Monthly Notices of the Royal Astronomical Society*, 408, 1029, (c) Journal compilation © 2010 RAS
- Morales, M. F., Hazelton, B., Sullivan, I., & Beardsley, A. 2012, *ApJ*, 752, 137
- Morales, M. F. & Wyithe, J. S. B. 2010, *Annual review of astronomy and astrophysics*, 48, 127, oise
- Paciga, G. et al. 2013, *Monthly Notices of the Royal Astronomical Society*, 433, 1427
- Parsons, A. et al. 2010, *The Astronomical Journal*, 139, 1468
- Parsons, A., Poher, J., McQuinn, M., Jacobs, D., & Aguirre, J. 2012a, *ApJ*, 753, 81
- Parsons, A. R. & Backer, D. C. 2009, *The Astronomical Journal*, 138, 219
- Parsons, A. R. et al. 2014, *ApJ*, 788, 106
- Parsons, A. R., Poher, J. C., Aguirre, J. E., Carilli, C. L., Jacobs, D. C., & Moore, D. F. 2012b, *The Astrophysical Journal*, 756, 165
- Poher, J. C. et al. 2014, *The Astrophysical Journal*, 782, 66
- . 2013a, *The Astrophysical Journal*, 768, L36
- . 2013b, *The Astronomical Journal*, 145, 65
- . 2012, *The Astronomical Journal*, 143, 53
- Pritchard, J. & Loeb, A. 2008, *Physical Review D*, 78, 103511
- Pritchard, J. R. & Loeb, A. 2012, *Reports on Progress in Physics*, 75, 6901
- Stefan, I. I. et al. 2013, *Monthly Notices of the Royal Astronomical Society*, 432, 1285

- Sullivan, I. S. et al. 2012, *The Astrophysical Journal*, 759, 17
- Thyagarajan, N. et al. 2013, *The Astrophysical Journal*, 776, 6
- Tingay, S. et al. 2013, *Publications of the Astronomical Society of Australia*, 30, 7
- Trott, C., Wayth, R., & Tingay, S. 2012, *The Astrophysical Journal*, 757, 101
- Vedantham, H., Shankar, N. U., & Subrahmanyam, R. 2012, *The Astrophysical Journal*, 745, 176
- Yatawatta, S. et al. 2013, *Astronomy & Astrophysics*, 550, 136
- Zheng, H. et al. 2014, eprint arXiv, 1405.5527

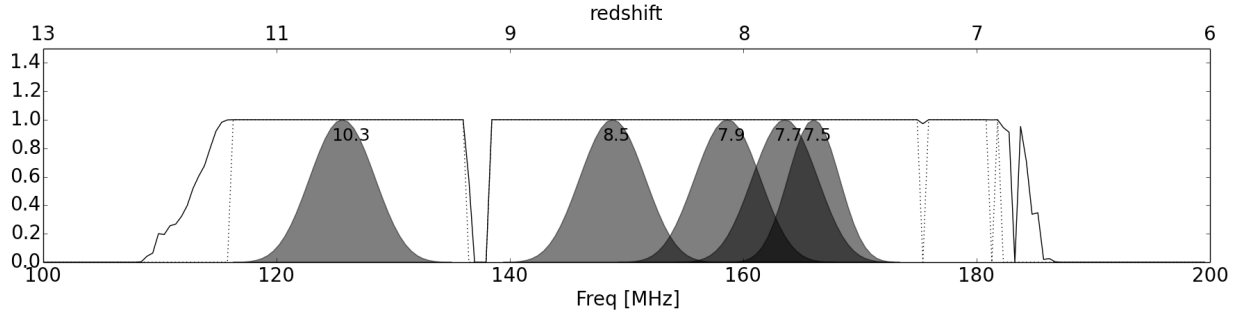


Fig. 1.— The average amount of data remaining after interference flagging over the 3 month period between Dec 2011 and March 2012 (black line) is quite high. Redshift bins (in grey, redshift center indicated with text label) are chosen to include spectral channels with uniform weight, i.e. no missing channels while maximizing coverage over the band. Redshift 7.68 is included for comparison with P14. Channels with no missing data are indicated by the dotted line, visible at the edge of flagged channels. Each redshift bin is 20 MHz wide, but weighted by a Blackman-Harris window function which heavily down-weights the outer 10MHz for a Noise Equivalent Bandwidth of 10MHz. The interference is almost exclusively dominated by two features: ORBCOMM satellites at 137MHz and an unidentified intermittent line emitter at 175MHz. The roll off at 115MHz is due the rising noise at low frequencies being incorrectly flagged as interference.

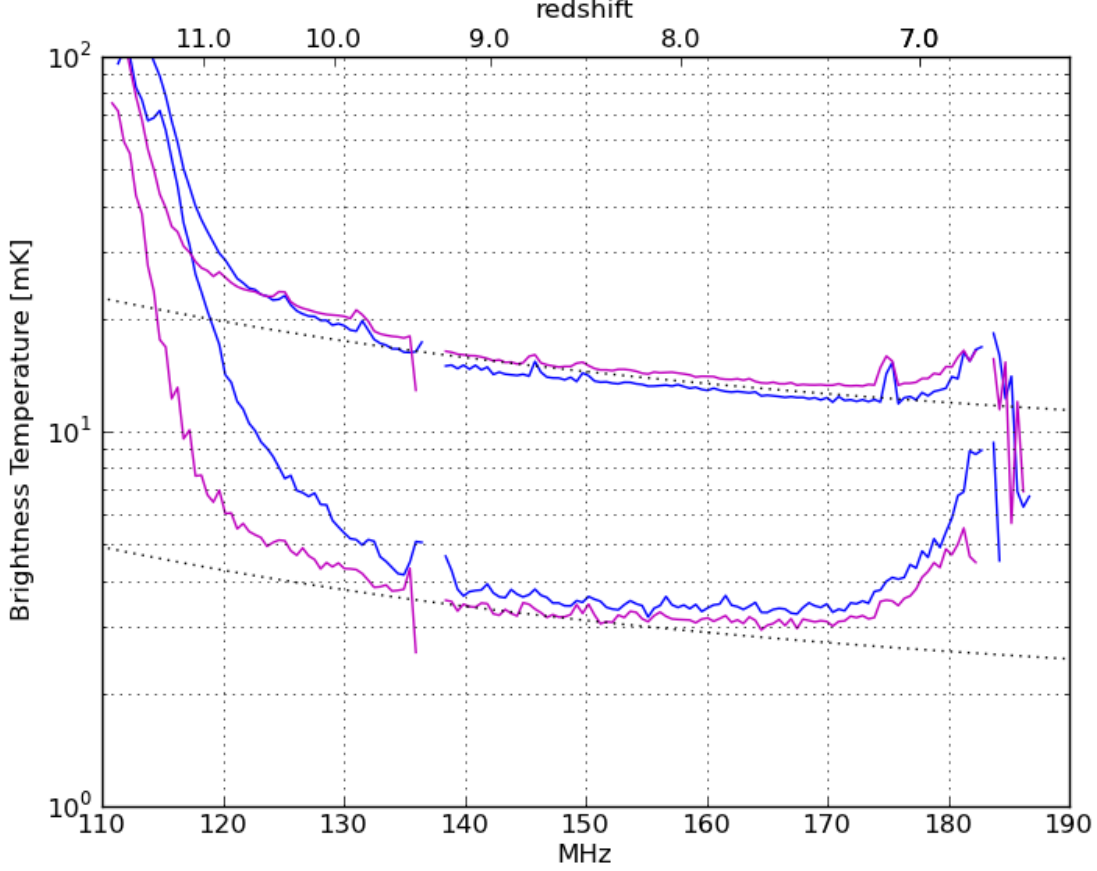


Fig. 2.— Root mean square (rms) noise before and after integrating to 10 minute LST bins (top and bottom sets of curves) indicating the rising significance of foregrounds as we take the last deep integration step. Noise is estimated by differencing adjacent frequencies (magenta) and between redundant baselines (blue), compared with an estimate of the theoretical noise level with a T_{sys} of 550K (dotted). The top three lines show noise after filtering foregrounds and binning into 40s long sidereal bins. At this noise level the frequency and baseline differences are roughly similar, both demonstrate the same small bumps of increased noise due to interference flagging and are consistent with noise over much of the band. The bottom three lines show the noise level after integrating up to the maximum fringe rate of 776s. The step between the top and bottom sets is the last coherent integration with noise largely decreasing by the expected factor $\sqrt{776/40}$ except in the difference between baselines (blue) which demonstrates a clear excess at all frequencies, particularly above redshift 10. With this last large jump in sensitivity we are now seeing the slight dominance of baseline covariance over the spectral derivative rms.

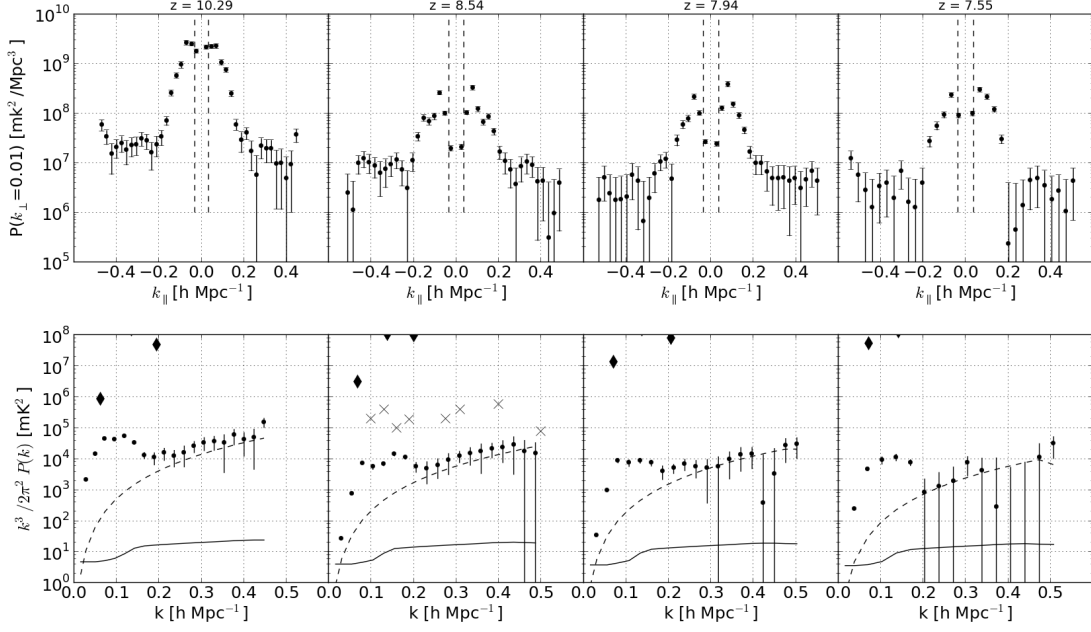


Fig. 3.— PAPER power spectra at four redshifts. On the top, P_k spectra (a simple units change from the raw delay spectrum) provide a useful diagnostic on foreground rejection, while on the bottom we plot in Δ^2 cosmological units, error bars are 2σ . Redshift increases left to right. All spectra have an effective bandwidth of ± 10 MHz covering the redshift span $\Delta z \approx 1421$ MHz (B/f^2) which ranges from 0.8 at $z = 10.3$ to 0.45 at $z = 7.4$. The noise curve (dashes) is calculated using the method described in Pober et al. (2013b) and indicates the 1σ confidence bounds on data points consisting purely of noise; 65% of uncorrelated noise like data points will lie below the curve. However, note the caveat that due to the weighting of the delay transform, adjacent k bins are 50% correlated. See Pober et al. (2014, 2013b) for a discussion of the approximations made in those calculations. The black line is a fiducial model at 50% ionization (Lidz et al. 2008). GMRT points from Paciga et al. (2013) indicated with 'x's and MWA points (also using 32 antenna) are black diamonds.

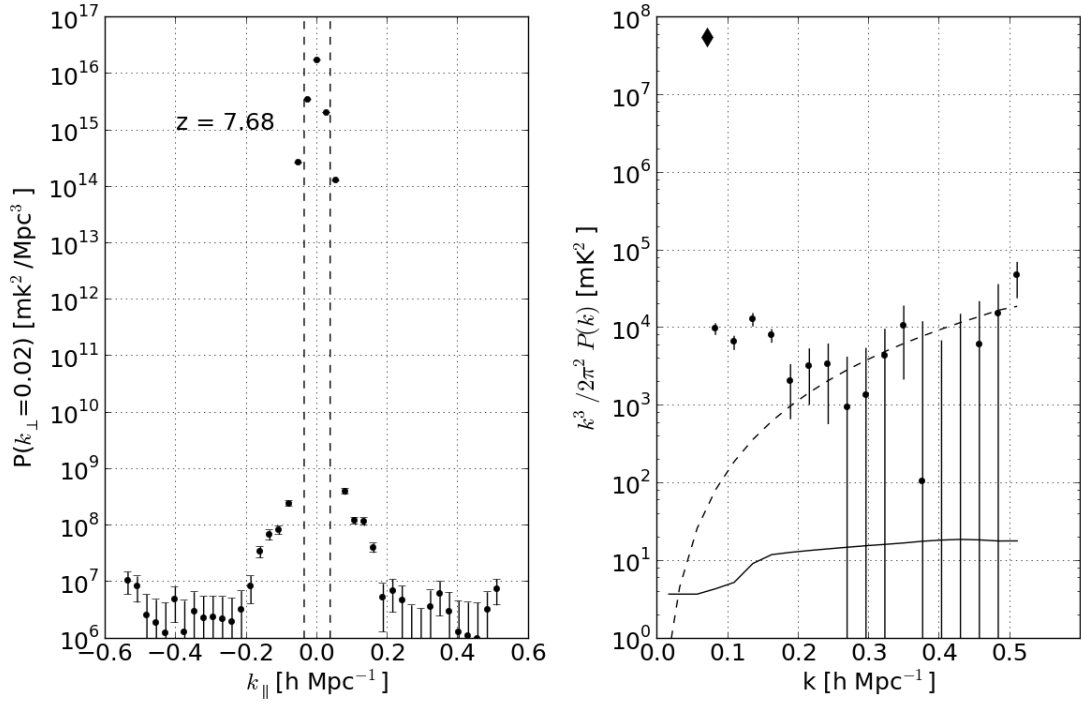


Fig. 4.— The redshift 7.68 bin has been reprocessed for comparison with the P14 result. See figure 3 for a detailed description of curves. Compare with figure 6 of P14. Note that the LST range processed here is 3 hours less than P14 for a small reduction in sensitivity but large reduction in foreground.

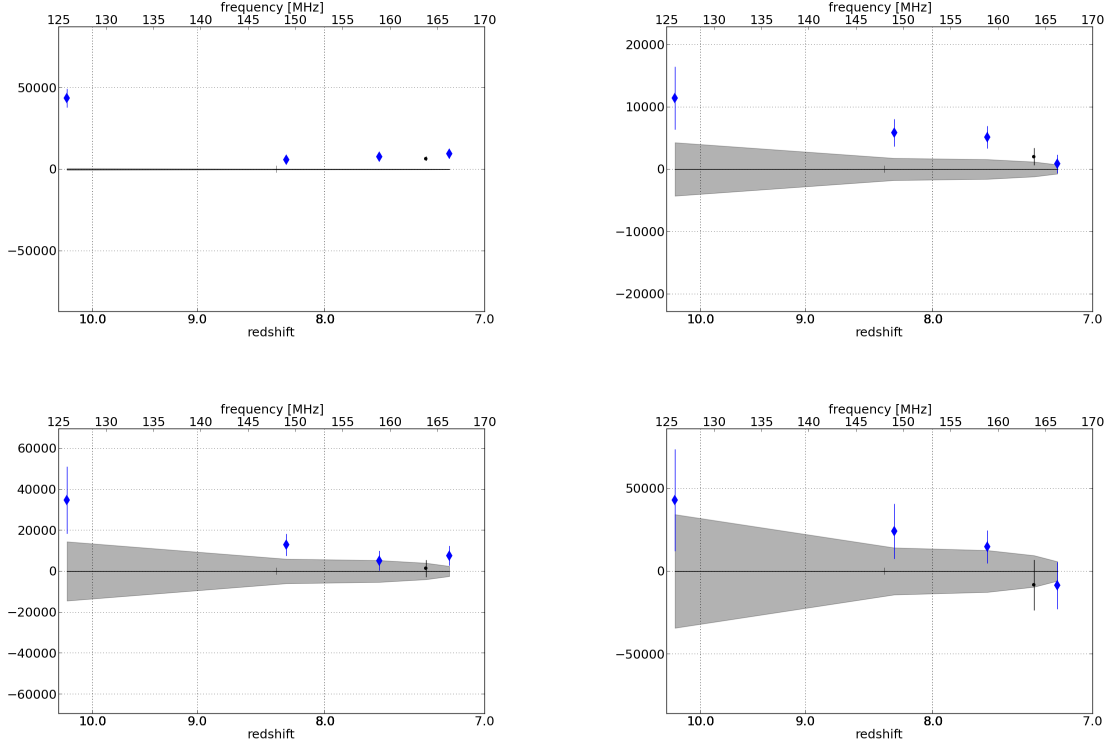


Fig. 5.— Power spectrum amplitude vs redshift at a selection of k modes. Left to right from top, $k=0.1, 0.2, 0.3, 0.4$ hMpc $^{-1}$. Parsons 2014 PAPER limit marked with thin black, this work marked with thick blue diamonds. The $k=0.1$ hMpc $^{-1}$ bin (top-left), which samples the delay spectrum at only 2x the maximum horizon delay is foreground dominated with a redshift dependence similar to the T_{rms} residual in Figure 2. The rest have amplitudes below the predicted noise level, but are not themselves perfectly consistent with noise, particularly at high redshifts. Though the points are all within the region predicted to be dominated by noise (grey) the variation between the redshifts and size of error bars suggests that a small residual signal is probably still present. The theoretical noise estimate is likely to be off by a small amount (see figure 3 and Section 4.2).